



Energy-loss correction in charge sharing events for improved performance of pixellated compound semiconductor detectors

S.L. Bugby^{a,*}, K.A. Koch-Mehrin^a, M.C. Veale^b, M.D. Wilson^b, J.E. Lees^a

^a Space Research Centre, Department of Physics & Astronomy, University of Leicester, LE1 7RH, UK

^b STFC Rutherford Appleton Laboratory, Harwell Campus, Didcot, OX11 0QX, UK



ARTICLE INFO

Keywords:

CdTe
Charge-loss correction
Gamma imaging
Energy resolution
Pixellated compound semiconductor detectors

ABSTRACT

The sharing of charge between multiple pixels can significantly degrade the energy resolution of small pixellated compound semiconductor detectors. This paper describes an energy calibration and reconstruction technique to correct for absorbed energy that is split over two neighbouring pixels, defined as bipixel events. Results were obtained with a 1 mm thick CdTe detector with 250 μm pixel pitch and an inter-pixel spacing of 50 μm , using the STFC HEXITEC ASIC.

The proportion of charge sharing events was found to be 54% for photons at 59.5 keV when applying a noise threshold of 3 keV. Across the energy range investigated, bipixels were the predominant shared event type and the absolute fraction of shared events was found to be dependent on the noise threshold used.

The reconstruction technique described reduces the degradation of energy resolution due to charge sharing in bipixel events compared to simple charge sharing summing techniques. This improved counting efficiency compared to using only isolated events and improved energy resolution compared to pixel addition techniques. When only isolated pixels were included, a FWHM energy resolution of 1.42 keV at 140.5 keV was achievable; inclusion of bipixel events using pixel addition results in an energy resolution of 3.33 keV whereas the reconstruction technique described here results in an energy resolution of 2.14 keV. When bipixel events are combined with single pixel events, the number of counts within the 140.5 keV photopeak of ^{99m}Tc increased by over 100%.

1. Introduction

Compound semiconductor detectors are widely used due to their high detection efficiency, energy resolution superior to many scintillator based detectors, and ability to operate at high temperatures and in extreme environments [1] in sectors as diverse as medical imaging (e.g. [2]) and astronomy (e.g. [3]).

Common semiconductor materials, such as CdTe and CdZnTe are preferable due to the high average Z number and therefore linear attenuation of their components and large bandgap which allows operation at room temperature. However, carrier mobility — particularly for holes — is low in these materials and this, along with material impurities and defects, can lead to charge trapping [4], polarisation [5], and a reduction in spectroscopic performance.

To overcome these limitations, many imaging detectors based on high Z materials (like CdZnTe) adopt a small pixel geometry in which the pixel pitch is small relative to detector thickness [6]. The process of signal formation in such a geometry is described by the Shockley–Ramo theorem [7]. A significant induced charge will only be formed on a small pixel when the charge carriers created by an interaction drift

close to the pixel. Assuming the majority of interactions occur far from the pixellated anode, the contribution of the easily trapped holes to the induced signal in detector will be minimal and good spectroscopic performance will be achieved.

While the use of a small pixel geometry can reduce the contribution of holes, it also introduces additional phenomena to the detector response that may need addressing. The interaction of photons with energies of the order of 100 keV result in the creation of charge clouds with widths of the order of 10 s of μm which then diffuse to larger diameters as the charge drifts towards the pixellated anodes. As the size of these charge clouds can be appreciable compared to that of the pixel pad and inter-pixel spacing, a significant number of interactions may result in charge induction and collection occurring across multiple pixels. Events where charge is collected on multiple pixels are described as ‘charge sharing’ and can result in a degradation of the energy resolution of a detector [8]. As the ratio of the pixel size to the detector thickness becomes smaller the number of interactions involving charge sharing increases until 100% are shared and the spectroscopic performance of the detector is compromised.

* Corresponding author.

E-mail address: s.bugby@le.ac.uk (S.L. Bugby).

As well as charge sharing effects, ‘depth of interaction’ effects can also act to degrade the energy resolution of the detector at high energies. For low photon energies the majority of interactions will occur close to the large planar cathode. At higher energies the mean free path of a photon in the semiconductor material may become similar or even exceed the thickness of the detector meaning interactions may create charge throughout the detector volume, including close to the pixelated anode. In the case of 1 mm thick CdTe, photons of energy 100 keV have mean free paths exceeding the detector thickness.

When interactions occur close to the anode the induced charge on the pixels is caused by the drift of the holes moving away from the anode in addition to the drift of electrons. The poor hole transport and trapping causes charge loss and hole tailing [9] which degrades the spectroscopic performance.

In order to maximise both the counting and spectroscopic performance of pixelated detectors the effects of charge sharing and charge loss require correction. In the case of charge sharing, the energy resolution of the detector may be preserved by charge-sharing discrimination (CSD) – discarding all multipixel events – although this reduces detector counting efficiency [10]. Alternatively, charge sharing addition (CSA) – where the signal above a noise threshold from adjacent pixels are combined – may be used but this is associated with an energy loss in multipixel events and this, along with the added contribution from readout noise results in a poorer energy resolution after reconstruction [11].

Counting efficiency is particularly important in medical imaging, where improved counting efficiency can lead to more statistically significant images, reduced imaging times, or lower patient dose. Energy resolution is also an important parameter, with better energy resolution allowing better discrimination of scattered events and an improvement in image contrast [12].

Both counting efficiency and energy resolution are important in dual-tracer imaging – such as ^{99m}Tc -sestamibi/ ^{123}I subtraction for parathyroid scintigraphy. For this technique, energy windows are reduced compared to those typically used clinically to limit cross talk to less than 5% [13], and even when these are optimised sensitivity loss can be as high as 15% [14]. The improved energy resolution of semiconductor detectors has been shown to result in better image quality in dual-tracer tests when compared to traditional scintillator-based gamma cameras [15], although charge sharing effects have been identified as degrading performance [16]. Improved charge sharing correction could improve the performance of semiconductor detectors further and potentially expand dual-tracer techniques to tracers with smaller photopeak separations.

The mechanisms behind charge sharing events in semiconductor detectors are the subject of significant research both through simulations (e.g. [8]) and through experiments where the precise location of incident photons are known and both electrons and holes are considered (e.g. [9]). In this paper, a charge correction method described by Abbene et al. [17] is applied to a 1 mm thick CdTe detector consisting of an 80×80 array of $250\ \mu\text{m}$ pixel pitch using the STFC HEXITEC ASIC [18], and extended to energies of interest to medical imaging. The calibration process is described fully, and a comparison to CSA reconstructions is provided. The calibration method described here can be performed by the standard end-user of a typical uni-polar (electron sensing) imaging detector to improve the device’s spectroscopic performance, and can be applied without an in-depth knowledge of the mechanisms of charge sharing.

2. Detector description

The High Energy X-ray Imaging Technology (HEXITEC) is a read-out application-specific integrated circuit (ASIC) and series of detectors that have been developed through a collaboration between multiple UK universities and the Science and Technology Facilities Council (STFC) to detect hard X-rays and gamma rays. The detector is coupled to the ASIC to perform spectroscopic observations, recording the

position and energy of all incident photons. The ASIC consists of an 80×80 pixel read-out array with a pitch of $250\ \mu\text{m}$ manufactured on a standard $0.35\ \mu\text{m}$ CMOS (complementary metal-oxide semiconductor) process [18], such that each ASIC pixel contains a charge amplifier, shaping amplifier and a peak track-and-hold circuit. Therefore, induced charge is converted to a voltage at the pixel level, allowing each pixel be readout in turn and their individual measurements of photon energy included in a full energy spectrum per pixel.

The primary detector used in this work is a CdTe semiconductor detector manufactured by AcroRad Ltd. which has been coupled to the HEXITEC ASIC. The design of the detector consists of a platinum planar cathode and pixelated aluminium anode on opposite sides of the CdTe semiconductor material. The CdTe sensor has a thickness of 1 mm and a $20\ \text{mm} \times 20\ \text{mm}$ collecting area. The anode is pixelated by an 80×80 array with a pixel electrode size of $200\ \mu\text{m}$ and an inter-pixel spacing of $50\ \mu\text{m}$. The CdTe is screen printed with silver epoxy to place a $\sim 120\ \mu\text{m}$ diameter epoxy dot on each of the 80×80 pixels. The ASIC has a gold stud placed on each of its bond pads and is then flip-chip assembled with the CdTe and cured at temperatures $< 120\ ^\circ\text{C}$.

The HEXITEC ASIC has previously been shown to have a mean pixel FWHM (full width at half maximum) energy resolution of 800 eV at 60 keV, and a minimum recorded resolution of approximately 600 eV [19]. This suggests that the performance of the detector system is material limited with an electronics noise contribution of the order of 500 eV.

The detector and ASIC module were mounted in a readout system with off-chip digitisation, an FPGA (field programmable gate array) for ASIC clocking and a gig-ethernet connection to a PC. An ASIC frame rate of 1.6 kHz was used for these experiments. The readout system controlled the detector temperature to $28\ ^\circ\text{C} \pm 1\ ^\circ\text{C}$ and applied a bias voltage of $-500\ \text{V}$ to the CdTe cathode. To avoid polarisation, the bias voltage was automatically refreshed by switching the bias to 0 V for 2 s once every minute. The control and data acquisition was conducted through a software graphical user interface (GUI).

Calibration and further analysis was then performed with custom written software developed at the University of Leicester in Python and IDL [20].

3. Detector calibration

The energy response of the detector was calibrated individually for each pixel. The detector was calibrated with sealed radioisotope sources of ^{109}Cd , ^{241}Am and ^{57}Co giving 7 photopeaks for calibration ranging from 14.4 keV to 136.5 keV as shown in Table 1. Additional peaks also visible in each spectrum (see Fig. 1) were not used for calibration. Sources were placed at a distance of 300 mm from the detector to ensure uniform illumination. Energies below a low energy noise threshold of 3 keV were removed before calibration.

The highest count rate was for the ^{241}Am source where an average frame occupancy (defined as percentage of pixels with energy above the set noise threshold) of 0.5% was observed. An occupancy of less than 11% would mean that, on average, no more than 1 event will be recorded in each 3×3 pixel block [19]. For occupancy rates considerably lower than this, we can assume the likelihood of a multipixel event occurring due to two adjacent events rather than charge sharing is very low.

Integration time was set at 1000 s to ensure constant temperatures and integrations were repeated until the primary photopeak maximum was at approximately 500 counts per pixel (statistical error in counts $< 5\%$). Only single pixel isolated events were used in the energy calibration process to ensure that the process was not compromised by the effects of charge sharing.

An approximate location for each photopeak was identified manually from the whole image energy spectrum. A Gaussian was then automatically fitted to each photopeak region for each pixel in turn. The centroid position (in ADU) and the standard error from the fit was

Table 1

Table of photopeak energies used in calibration. Multiple peaks (i.e. $K_{\alpha 1}$ and $K_{\alpha 2}$) have been combined into a single peak energy taking into account their relative intensity where these cannot be resolved. The range of energies included in each photopeak is shown as a standard error, this is set to a nominal value of 10 eV when individual peaks have not been combined. The occupancy is the mean percentage of pixels in each frame which are above the noise threshold.

Source	Source activity (MBq)	Photopeak energies (keV)	Acquisition time (s)	Occupancy
^{109}Cd	84.9	22.00 ± 0.10	1000	0.4%
		24.90 ± 0.01		
		88.00 ± 0.01		
^{241}Am	351.7	59.54 ± 0.01	1000	0.5%
^{57}Co	51.7	14.40 ± 0.10	7000	0.2%
		122.10 ± 0.05		
		136.50 ± 0.10		

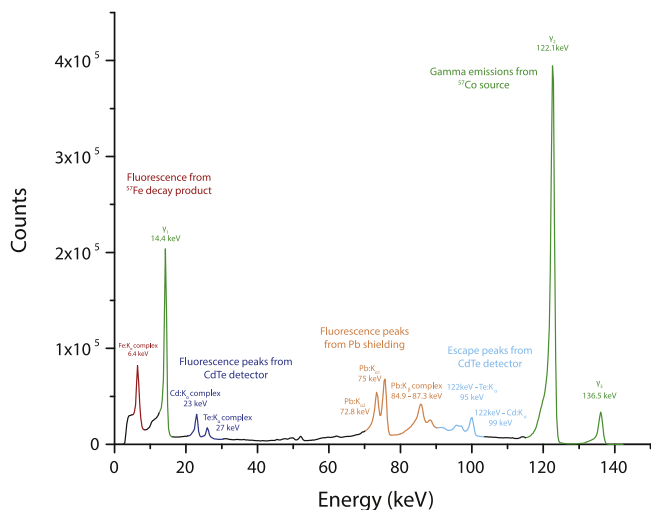


Fig. 1. Whole-detector calibrated energy spectrum for isolated events from a ^{57}Co source taken at 28 °C. Fitting Gaussian distributions to the gamma emissions peaks (Table 1) gives FWHM energy resolution values of 0.935 keV (γ_1), 1.3 keV (γ_2) and 1.21 keV (γ_3).

recorded for each pixel at every photopeak. A linear fit was performed on the photopeak energies in keV and ADU centroids of the fitted peaks. This calibration was then used to convert ADU to energy on a per pixel basis before any further analysis was performed.

Pixels were excluded from further analysis if they exhibited poor energy linearity ($R^2 < 0.97$) or if less than half of the photopeaks were successfully fitted. In general, the energy linearity of the individual pixels was very good, with a mean R^2 fitting statistic of 0.999908, and a minimum value of 0.99902, excluding removed pixels. Hot pixels – defined as those recording a signal above the noise threshold (90 ADU or approximately 3 keV) in more than 1% of frames of a dark image – were also excluded. This resulted in the exclusion of 22 pixels (0.34% of the imaging array) from analysis.

During charge sharing analysis (see Section 4), all events adjacent to an excluded pixel have been discounted. Events on the edge of the detector, or adjacent to the edge of the detector, were also excluded. This is to limit false positives or negatives in multipixel events.

Fig. 1 shows a ^{57}Co energy spectrum after calibration with multiple peaks separable and identifiable. This is a whole-detector spectrum containing summed spectra from each pixel not excluded during the calibration process. The energy resolution of 1.3 keV at the 122 keV photopeak is in line with that previously reported in the literature e.g. 1.2 keV at 122 keV [19].

4. Multi-pixel events

A single frame of HEXITEC data – an example of which is given in Fig. 2 – can provide the spectroscopic data of a number of events.

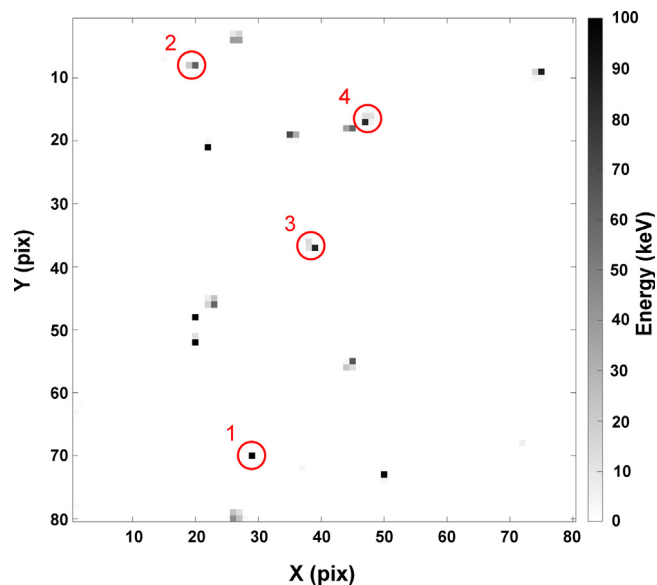


Fig. 2. A single frame of spectroscopic data from a ^{57}Co sealed source. Examples of different event types have been labelled, 1: isolated, 2: bipixel, 3: tripixel, 4: quadpixel.

Charge may be constrained to a single pixel – resulting in an isolated event – or shared over two or more pixels via the mechanisms described in Section 1. Examples of some event types are labelled in Fig. 2, with events containing 5 or more pixels also possible.

When spectroscopic response is the most important imaging characteristic – such as when differentiating between two similar energies – it is common to use only isolated events (CSD) – as in Fig. 1. Where efficiency is more important than energy resolution – as in medical imaging – multipixel events can be included in the spectrum (CSA). The HEXITEC system records raw energy and position information which can then be reconstructed using either CSD or CSA algorithms within the HEXITEC software, or analysed separately however the user requires.

Fig. 3 shows

1. a raw energy spectrum which includes every pixel individually in the spectrum
2. an isolated event spectrum (equivalent to CSD reconstruction)
3. spectra with contributions from multipixel events reconstructed with CSA.

Counts are significantly higher at lower energies in the raw spectrum as multipixel events are split into multiple lower energy events. The CSA technique reduces noise when compared to raw data, and compared to the isolated spectrum it is clear that each addition of more event types to the total spectrum improves counting efficiency while simultaneously degrading energy resolution.

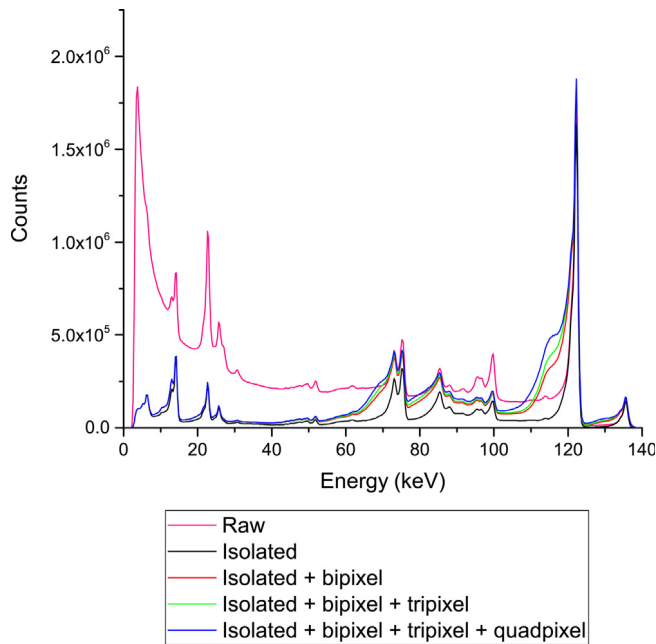


Fig. 3. Whole-detector calibrated pixel addition energy spectra from ^{57}Co source with different event types included in a total spectrum. Linear events have been excluded for tri- and quadpixels. Other event types are not included due to low incidences (see Fig. 4 for description of event types).

4.1. Multipixel analysis

An event analysis algorithm written in IDL – based on previous work at the University of Leicester (G Hansford, Personal Communication, 2017) – was developed to identify and catalogue multipixel events across the detector.

Pixels are said to be part of the same event if;

- They are in the same frame.
- They are adjacent (excluding diagonally adjacent) to one another

Diagonally adjoined events are counted as two separate events (G Hansford, Personal Communication, 2017). When diagonally adjoined events were included, a significant number of events were seen with double the expected photopeak energy – suggesting two distinct events were being counted as one. However, it is likely that excluding these events will exclude some instances where a fluorescent photon has travelled to a diagonally adjacent pixel before absorption — this will be investigated further in the future.

Each event is then characterised by the number of pixels it contains and its shape with some examples of event classifications shown in Fig. 4.

4.2. Proportion of multipixel events

The multipixel analysis algorithm was applied to the ^{109}Cd , ^{241}Am and ^{57}Co observations detailed in Table 1, along with an observation of a 414 MBq ^{55}Fe radioisotope source (3600 s acquisition time, 0.2% occupancy) and a 188.3 MBq $^{99\text{m}}\text{Tc}$ liquid radioisotope source in a 10 ml vial (1800 s acquisition time, 0.4% occupancy) using the same experimental arrangement.

For each observation, a spectrum of each event type was created (energy response is discussed in Section 4.3). From this, the number of events of each type was calculated for a range of energies. Due to the shifting and broadening of the energy peak for multipixel events, the energy windows associated with each photopeak was varied. The energy response of different pixel types is discussed in more detail in the

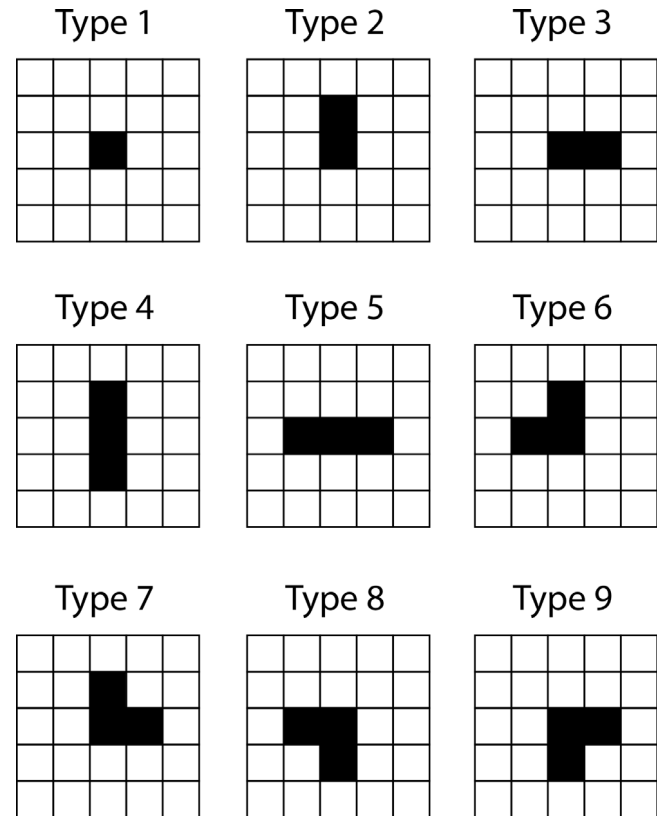


Fig. 4. Event shapes and their designations for isolated, bi- and tri-pixel events.

following section. Table 2 tabulates each energy that was investigated, along with the energy range that was said to contribute to that peak for each event type. The fraction of events within the energy window that were due to each event type are shown in Fig. 5, which was produced using a low energy noise threshold of 3 keV. Errors associated with Poisson statistics and the positioning of the energy windows are estimated at <2%.

Charge sharing is an inherent property of a pixelated detector, and is dependent on a number of parameters relating to the design of the detector itself such as the pixel pad width, inter-pixel gap, sensor thickness and operating bias voltage. At energies <26 keV these detector parameters are the sole determinant of charge sharing rates in a CdTe sensor. At energies >26 keV (the K-edge of Cd) the generation of fluorescence photons which have ranges of the order of 100 μm in the sensor material further supplement the geometric charge sharing rates.

As X-ray energies increase further from tens of keV to hundreds of keV, the increase in the number of events affected by Compton scattering and the increase in the size of charge clouds will also lead to an increase in the number of multi-pixel events. The majority of the multipixel events within the energy range investigated are bipixels. The proportion of these increases with increasing energy until 59.5 keV where it becomes approximately stable at 39% – similar to the incidence of isolated events at these energies. The contribution of events containing more than two pixels also increases with increasing energy as would be expected.

When a photon is absorbed in the detector, a charge cloud is generated with an initial size dependent on the energy of the photon. As this charge cloud drifts towards the detector anode its size will increase due to diffusion effects — this increase is dependent on drift time and therefore dependent on the distance between the initial interaction and the anode. If the size of the initial charge cloud was the dominant factor, it would be expected that the proportion of multipixel events

Table 2

Energies used to calculate proportion of multipixel events. The 74 keV energy analysed from the ^{57}Co acquisition data occurs due to Pb fluorescence from shielding in the experimental setup. Multiple peaks (i.e. $K_{\alpha 1}$ and $K_{\alpha 2}$) have been combined into a single peak energy taking into account their relative intensity where these cannot be resolved. The range of energies included in each peak is shown as a standard error, this is set to a nominal value of 10 eV when individual peaks have not been combined.

Source	Energy (keV)	Energy window (keV)				
		Isolated	Bipixel	Tripixel	Quadpixel	>Quadpixel
^{55}Fe	5.95 ± 0.01	4–11	4–11	4–11	4–11	4–11
^{109}Cd	23.50 ± 1.50	13–28	12–28	13–28	14–28	13–28
	88.00 ± 0.01	77–92	75–91	73–91	73–91	71–90
^{241}Am	59.54 ± 0.01	39–63	38–63	37–63	37–64	49–62
	14.10 ± 0.10	9–16	6–16	6–15	11–16	11–16
^{57}Co	74.00 ± 1.00	63–77	60–76	59–75	59–73.5	61–73
	122.10 ± 0.05	105–126	105–126	105–125	105–124	99–122
	136.50 ± 0.10	126–140	125–140	124–140	123–140	122–140
$^{99\text{m}}\text{Tc}$	140.50 ± 0.10	125–145	120–145	120–145	118–145	120–145

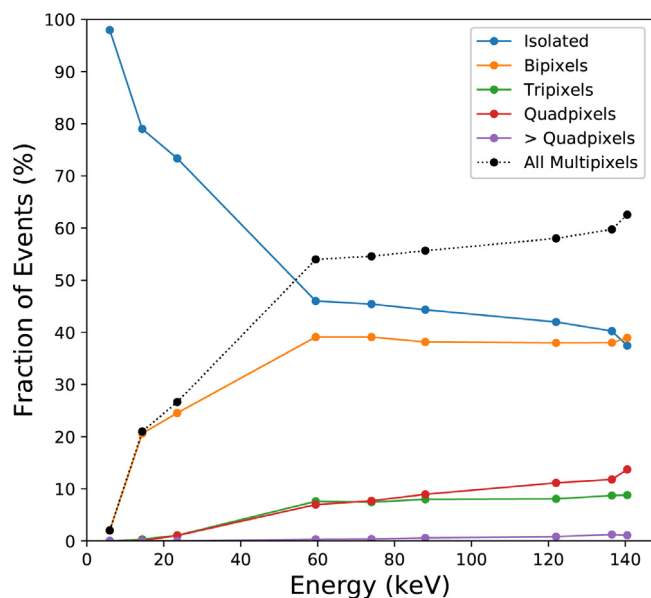


Fig. 5. Fraction of individual event types and all multipixel events of all recorded events across the whole detector. Each data point is associated with a photopeak at that energy. The dashed line shows ‘all multipixels’ which includes all event types except isolated events.

would continue to increase at higher energies. Fig. 6 shows the mean interaction depth for photons absorbed in a 1 mm block of CdTe, which levels off at higher energies due to the maximum possible interaction depth of 1 mm and the extent of diffusion effects would be expected to follow a similar pattern. Therefore the results in Fig. 6 are consistent with previous findings that diffusion is the dominant mechanism in charge sharing [21] at the energies investigated in this work.

4.2.1. Effect of applied noise threshold

The initial steep increase of bipixel events at low energies (<20 keV) is in part due to the applied noise threshold of 3 keV. At lower energies, energy shared with adjacent pixels is more likely to be lower than this threshold leading to a failure to identify true charge sharing events.

It must be noted that the applied low energy noise threshold has an effect on the number of shared events that are recorded. Fig. 7 shows the percentage of all shared events and only bipixel events for three different line energies when the analysis was done with different noise thresholds. In each case, the occupancy per frame was observed to stay below 2%. The percentage of shared events at 122 keV ranges from 66.5% at a noise threshold of 1.5 keV to 53% when applying a 5 keV threshold. Bipixels remain the dominant multipixel event ranging from 32.7% to 39% respectively. For higher photon energies the fraction

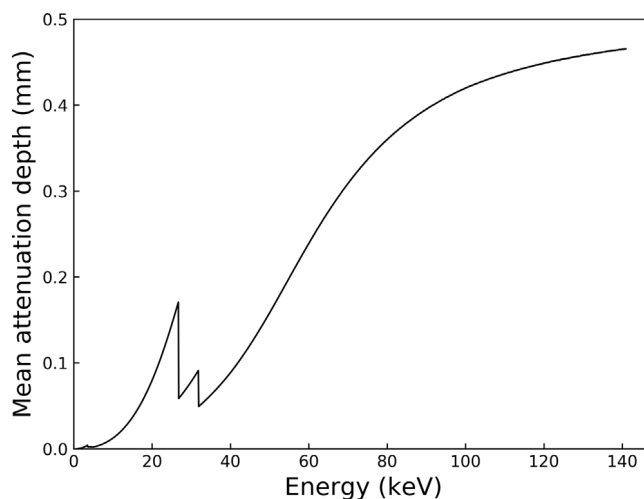


Fig. 6. Mean attenuation depth for photons in a 1 mm block of CdTe. Attenuation coefficients from NIST XCOM database [22]. Each data point ranging from 1 keV to 141 keV in steps of 0.1 keV was calculated using a simple Monte-carlo simulation which determined the attenuation depth of each of the 10^7 incident photons which were attenuated within the 1 mm thick CdTe.

of bipixel events decreases with smaller noise threshold as they are replaced by tripixel, quadpixel and even larger pixel events.

The effect of noise threshold can also be seen in the energy spectrum as shown in Fig. 8. Here, only isolated events (CSD reconstruction) are shown. The increase in the shoulder on the LHS of the photopeak with increasing noise threshold shows that some ‘energy loss’ is due to the removal of a low energy pixel from a bipixel event. However, there is a trade off when lowering the noise threshold as the number of events within the photopeak decreases (due to a reduction in isolated events overall) and an increase in low energy noise events – events below 5 keV account for 91.5% of all events when a 1.5 keV threshold is used, but only 2.2% of events when using a 3 keV threshold – which can interfere with analysis. The appropriate noise threshold setting is therefore a trade-off, which will depend on the performance of each system’s readout electronics. The 3 keV noise threshold used here was chosen based on a dark noise calibration of the device used, and the optimal setting to both limit pick-up cross talk in the electronics while reducing charge loss will vary between devices.

Veale et al. [19] give a proportion of shared events at around 55% at 59.5 keV and 56% at 122 keV when applying a noise threshold of 2 keV. This is slightly lower than the values found in this work and may be due to the variation in energy window for different event types used here, which was based on the spectrum for each type. Differences in noise performance between different detectors or experimental arrangements are also expected to impact the proportion of shared events.

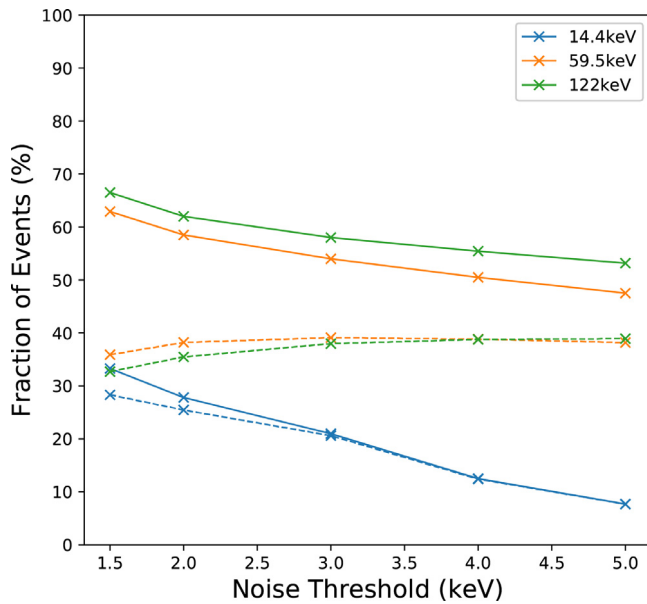


Fig. 7. Fraction of events as a function of applied noise threshold. Solid lines represent all events for which charge was shared across multiple pixels and dotted lines show the fraction of only bipixel events.

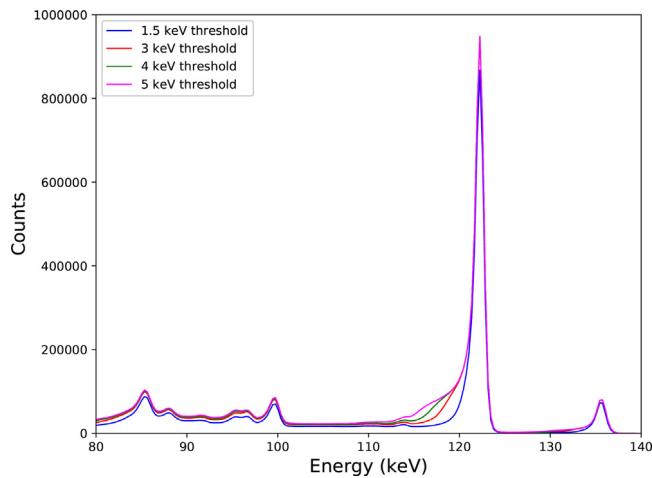


Fig. 8. Isolated event spectra of a ^{57}Co source with different noise thresholds applied.

4.3. Energy response of multipixel events

In Fig. 9, the energy spectrum of a number of event types are shown for a ^{57}Co source with a 3 keV noise threshold. These have been reconstructed using CSA. Inline tripixel (e.g. type 4 and 5 in Fig. 4) and quadpixel events, and events containing more than four pixels, have been excluded due to low incidences of these event types ($< 1\%$ of events). All other shaped quadpixel events have been combined into a single spectrum.

Photopeaks in spectra produced by multi-pixel events are broader with centroids at lower energies than spectra from single-pixel events — this will be discussed in more detail in the following sections. A distinct shoulder/splitting of the peak is seen in bipixel event spectra in Fig. 9. This is believed to be due to the combination of two event types — fluorescence and charge sharing (see Section 5.1).

The energy resolution of multipixel events will be limited by the readout noise of the detector electronics which will contribute in quadrature for each pixel additionally included. With an energy resolution of 1.21 keV for isolated 122.1 keV photon events (Fig. 1), a bipixel

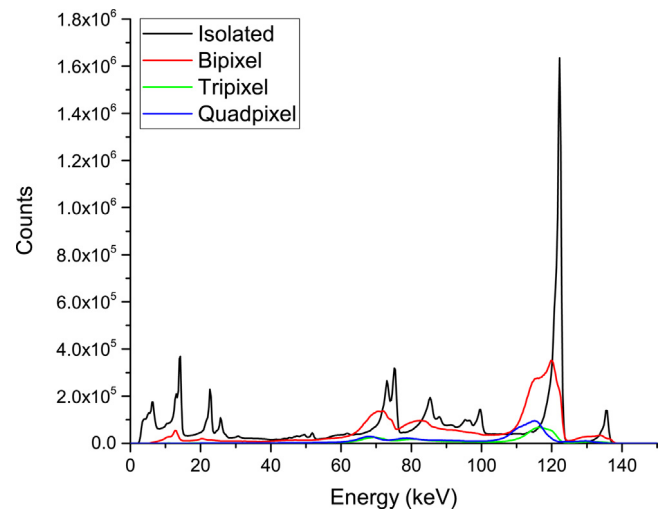


Fig. 9. Whole-detector calibrated pixel addition energy spectra for different event types from ^{57}Co source. Linear events have been excluded for tri- and quadpixels. Other event types are not shown due to low incidences.

event would be expected to have an energy resolution in the region of 1.3 keV if only the extra read noise from the additional pixel is taken into account. A considerably larger increase in energy resolution is seen in Fig. 9 suggesting that, for these energies, the additional contribution of electronic readout noise is minor in comparison to other effects. This is the case even when fluorescence and charge sharing events are separated as in Section 5.1

5. Bipixel event calibration

To investigate a reconstruction technique for bipixel events, the energy split between bipixel events has been plotted in Fig. 10 — for photopeaks from ^{241}Am and ^{57}Co sources. In both cases, distinct bright spots are visible that correspond to locations of four fluorescence peaks — Cd (K_{α} :23 keV, K_{β} :26 keV) and Te (K_{α} :27 keV, K_{β} :31 keV). In these cases, the split pixel events are not due to charge diffusion, but due to a fluorescence photon escaping and being captured in an adjacent pixel.

Apart from these features, there is a strong relationship between the energy recorded in each pixel. If there was no charge loss, this relationship would be expected to be a straight line. Instead, the data displays a slight curve indicating that the more evenly the energy is split between pixels the greater the charge loss. The charge loss can be partially attributed to loss in the inter-pixel gap. The electric field in this region will have a lower magnitude and the path of the drifting charge may not always be perpendicular to the electrode. The result is a change in both drift length and drift time resulting in additional charge loss compared to in-pixel regions. Depth of interaction effects also contribute to charge loss particularly at higher energies [9]. The charge loss seen here will be a combination of both effects.

Following work by Abbene et al. [17] a fit was performed for each calibration photopeak in Table 1. This assumes that given an incoming energy E and a recorded energy of P_1 in one pixel and P_2 in its adjacent pixel, an empirical relationship can be given as;

$$P_1 + P_2 = E - A \left(1 - \left[\frac{P_1 - P_2}{P_1 + P_2} \right]^2 \right) \quad (1)$$

where A is a parameter fitted to experimental results.

Fig. 11 shows an example for this fit for the 22.1 keV ^{109}Cd photopeak, and the relationship between photopeak energy and fit parameter A . Fig. 11 corresponds well with the plot for a 1 mm thick CdZnTe detector illuminated with an uncollimated ^{109}Cd source in Abbene

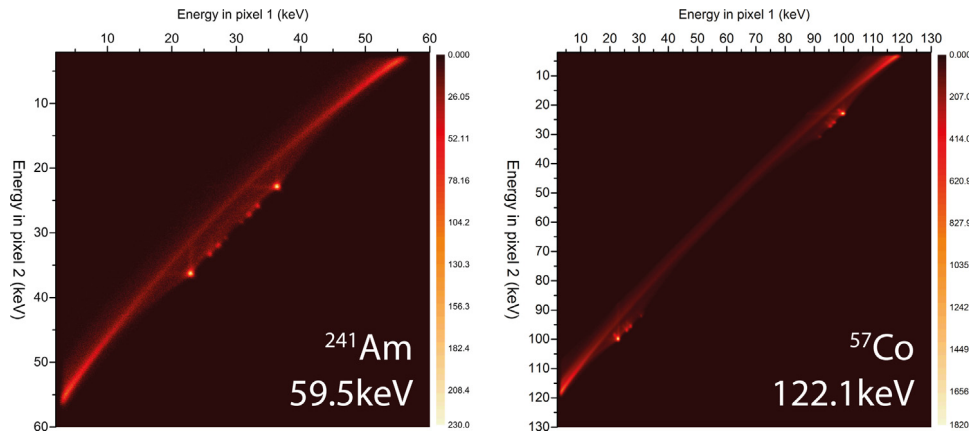


Fig. 10. Illustration of energy split between bipixel events. All events identified as bipixels within energy ranges of 50 keV–60 keV (^{241}Am 59.5 keV photopeak) and 110 keV–125 keV (^{57}Co 122.1 keV photopeak) are included. The energy of the pixels within each event are plotted against one another.

et al. [17], although Fig. 11 shows a broader spread as it includes contributions from all pixels in the detector, whereas Abbene et al. show data from a single pixel amongst other differences. Events containing pixels within a 1 keV energy window of either Cd or Te fluorescence energies were excluded from the fitting.

The fit produced in this technique (line in Fig. 11:left) is dependent on a number of factors including the range of energies that are included in the fitting and the energy window used to exclude fluorescence events. The fit could also be greatly improved if an ideal monochromatic source without a complex spectrum could be used as this would be expected to reduce the noise in the data. These factors contribute to the estimated errors shown in Fig. 11:right, these are larger for higher energies due to the greater complexity of the spectra and the broadening of the energy peaks.

Abbene et al. [17] show a linear fit between energy and A for a 2 mm thick CdZnTe detector with energies up to 40 keV investigated. Fig. 11 is in agreement with Abbene et al. showing similar linear relationship for energies ≤ 88 keV, however a non-linear relationship is seen over the full energy range studied.

A linear fit to the full data set had a fit statistic $R^2 = 0.9350$ compared to $R^2 = 0.9986$ for a quadratic relationship (of the form $A = XE^2 + YE$).

Using the quadratic relationship, the incident energy resulting in a bipixel event can then be calculated using only the signal in each pixel through solving the quadratic equation;

$$\left(1 - \frac{P_1 - P_2}{P_1 + P_2}\right)^2 (Y + 1) E - \left(1 - \frac{P_1 - P_2}{P_1 + P_2}\right)^2 X E^2 - (P_1 + P_2) = 0 \quad (2)$$

The parameter A is associated with the difference between the actual and reconstructed energy, and the relationship shown in Fig. 11:left suggests that the amount of energy lost begins to level off at higher energies.

Energy loss due to charge sharing is due both to charge loss in the inter-pixel gaps [17] – which may have some depth component due to diffusion – and to depth of interaction effects [9]. As shown in Fig. 6, the mean depth of interaction varies with energy and levels off at higher energies as it becomes limited by the finite thickness of the detector – a similar pattern to that seen in Fig. 11. Under the current experimental setup, depth of interaction is not known – it is hoped that future experimental and simulation work will be able to separate and quantify the contribution of each process.

5.1. Treatment of fluorescence events

As shown in Fig. 10, fluorescence events should be treated separately to events showing geometric charge spreading. For fluorescent

bipixel events, both the incident photon and subsequent fluorescence photon are likely to have deposited their charge within the central region of their pixel. As such, they do not suffer from charge loss in the inter-pixel region and should be reconstructed using conventional CSA.

Bipixel events were identified as being due to fluorescence if either of the pixels contained energy within a set energy window of Cd (K_α :23 keV, K_β :26 keV) and Te (K_α :27 keV, K_β :31 keV) fluorescence peaks. However, as some events caused by geometric charge spreading will also contain pixel energies in this region, the size of the energy window used impacts the energy reconstruction significantly. Fig. 12 illustrates the effect of the fluorescence energy window width on the resultant spectra.

Where fluorescence events are under-identified – as with the fluorescence window of 0.5 keV in Fig. 12 – a peak can be seen to the RHS of the main photopeak. This is due to fluorescence events being treated as charge spreading events and so having their reconstructed energy increased by Eq. (2). Conversely, if fluorescence events are over-identified – as with the fluorescence window of 4.7 keV in Fig. 12 – a peak can be seen to the LHS of the main photopeak. This is due to charge sharing events which should have their energy increased by Eq. (2) instead being treated as fluorescence.

To determine the optimum energy window, reconstructions were performed using fluorescence window widths of 0.5 keV to 4.7 keV at 0.3 keV intervals. A Lorentzian curve (chosen due to the long tails seen on reconstructed spectra) was then fitted to the photopeak for each reconstruction and the Adj. R^2 fit statistics were compared. The best fit was found for an energy window of 1.1 keV, which has been used in all reconstructions below.

When a known photopeak energy is of interest, it is possible to constrain the definition of fluorescence events further. As both the possible fluorescence energies and possible escape peak energies (calculated as photopeak energy – fluorescence energies) are known, an energy window can be applied to both pixels in a bipixel event (2D energy windowing). In this case, a 1.7 keV energy window was found to produce the best reconstructions. This technique provides better identification of fluorescence events, and so better energy reconstructions (see Table 3), however cannot be practically applied across a whole spectrum. In medical imaging, where energies of interest are well defined, a 2D fluorescence window would be appropriate.

5.2. Results of calibration

Fig. 13 compares the energy spectrum of bipixel events reconstructed using CSA and Eq. (2) (with a 1.1 keV 1D energy window used to identify fluorescence events). This reconstruction shows significant improvement over the pixel addition technique. The peak centroid for

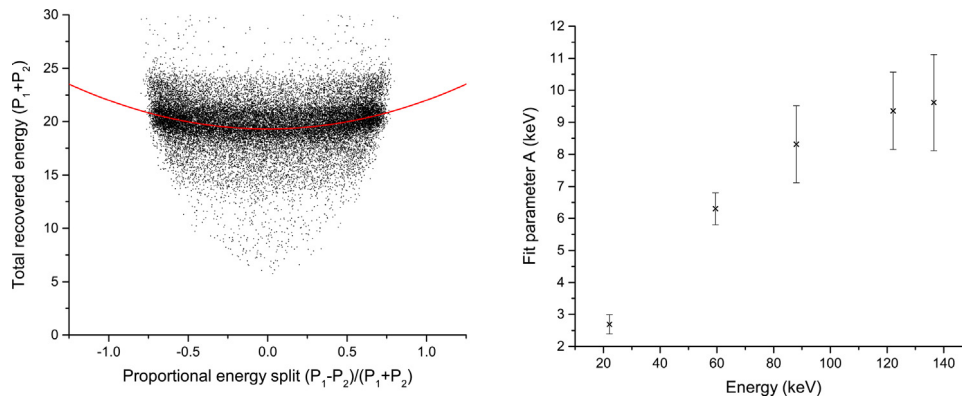


Fig. 11. Left: Relationship between proportional energy split and total recovered energy for 22 keV¹⁰⁹Cd photons. Line shows fitted relationship from Eq. (1) with $R^2 = 0.9986$. Right: Relationship between photopeak energy and fitted parameter A (as defined in Eq. (1)).

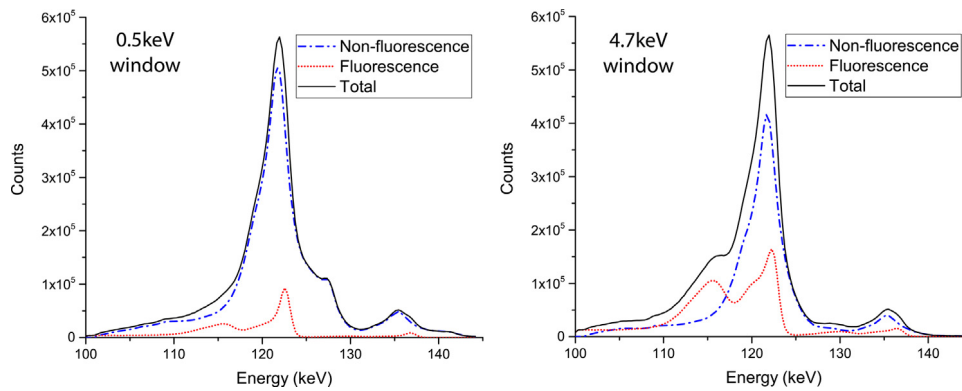


Fig. 12. Reconstructions of bipixel events from the⁵⁷Co photopeak. Non-fluorescence events are reconstructed using Eq. (2) and fluorescence events are reconstructed using pixel addition. The total spectra combine both fluorescence and non-fluorescence events. The fluorescence window width was Left:0.5 keV and Right:4.7 keV.

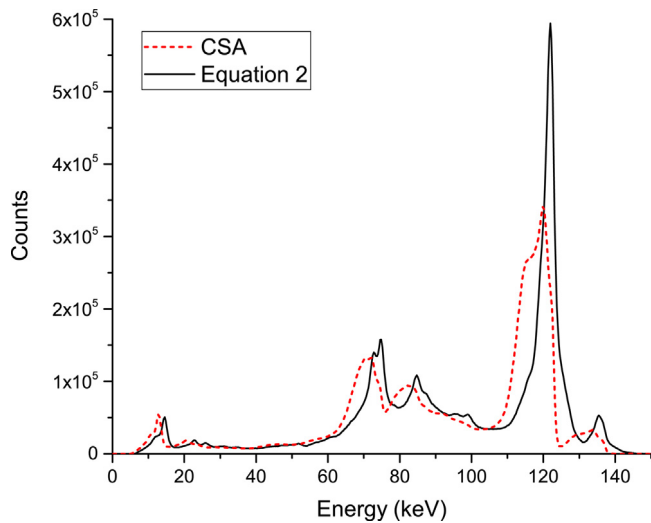


Fig. 13. Whole-detector bipixel energy spectrum from⁵⁷Co source reconstructed using the pixel addition technique or Eq. (2).

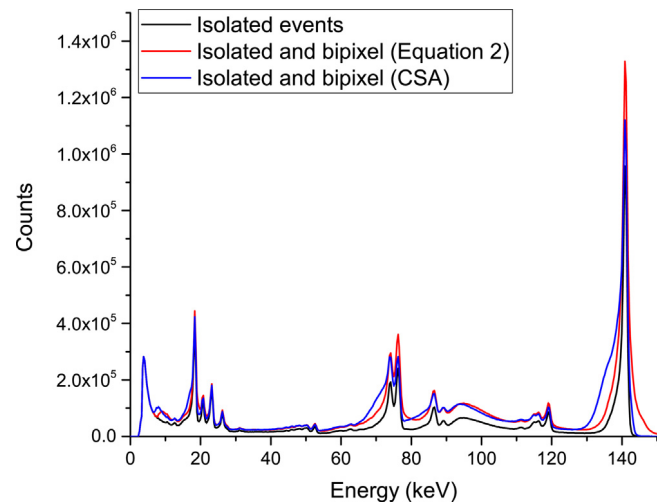


Fig. 14. Comparison of whole-detector^{99m}Tc spectra for isolated events, and isolated and bipixel events reconstructed using CSA or Eq. (2).

the 122 keV photopeak was at 117.6 keV using pixel addition with a 9.7 keV FWHM, and this improved to a centroid at 121.1 keV with a 4.6 keV FWHM. At lower energies, peaks can now begin to be separated which were previously entirely convolved (e.g. Pb fluorescence at ~75 keV).

In Fig. 14 Eq. (2) has been applied to bipixel events which are then combined with isolated events for a^{99m}Tc source – an important isotope

in medical imaging and one which was not used during the initial calibration steps described here. A 1.1 keV 1D fluorescence energy window was used. Table 3 compares spectra of isolated events only and isolated and bipixel events combined with bipixel reconstructions using either CSA or Eq. (2). Table 3 also compares the performance of Eq. (2) when 2D fluorescence windowing with a 1.7 keV window is used (not shown in Fig. 14).

Table 3
Comparison of parameters for 140.5 keV ^{99m}Tc photopeak for different spectra types.

Parameter	Isolated	Isolated and bipixel (CSA)	Isolated and bipixel 1.1 keV 1D fluorescence window (Eq. (2))	Isolated and bipixel 1.7 keV 2D fluorescence window (Eq. (2))
FWHM (keV)	1.42	3.33	2.14	2.02
Counts within 10% (5%) energy window	6.5×10^6	12.4×10^6	13.0×10^6	12.9×10^6
Counts within 5% (2.5%) energy window	6.1×10^6	10.1×10^6	11.3×10^6	11.4×10^6

Scuffham et al. [23] previously reported an energy resolution of 1.27 keV at 140.5 keV using a CSD algorithm and this is similar to that seen here for isolated events. Inclusion of bipixel events through either reconstruction method approximately doubles the number of counts within the photopeak although this does come at a cost to energy resolution.

With the CSA method, inclusion of bipixel events more than doubles a fitted FWHM energy resolution from 1% of the photopeak energy to 2.4%. If fluorescence events are included in the reconstruction as shown in Fig. 14, Eq. (2) results in an energy resolution of 1.5%, whereas if they are excluded the resolution is 1.3%. However, excluding these events reduces the number of counts within the photopeak by 12%–14% (depending on the photopeak window used). When fluorescence events are identified using a 2D window, energy resolution is slightly improved to 1.4%.

For medical imaging, where counting efficiency is often a limiting factor in imaging quality, the ability to include additional events is always significant. The improved energy resolution described here compared to a typical large field of view clinical camera (approx. 10% at 140.5 keV for NaI:Tl-based scintillator cameras [12] and 5% for existing CdZnTe systems [24] could improve scatter rejection and cross talk when used for dual-tracer imaging. However, the sensitivity of a NaI:Tl detector to 140.5 keV photons is approximately 100%, and that of existing CdZnTe systems of the order of 70% [24] compared to a theoretical maximum of around 30% for 1 mm CdTe. Extending this calibration process to thicker CdTe or CdZnTe detectors may potentially improve energy resolution performance for clinical imaging. Alternatively, this calibration could ensure that no more counts than necessary are excluded – the ability to increase photopeak counts by 100%, while maintaining energy resolution could improve performance in applications where high energy resolution is required but count rates are still a limiting factor such as baggage handling.

6. Conclusions

This paper describes a calibration technique to determine the empirical relationship between pixel value ratio in bipixel events and initially deposited energy, which may be then used to reconstruct energy in bipixel events as an alternative to the CSA technique.

Multipixel events form a significant proportion of events for small pixel detectors even at relatively low energies <100 keV. Of these events, bipixel events are the most common and are almost as likely to occur as isolated events for energies over 60 keV. Including multipixel events in analysis degrades energy resolution, however excluding them decreases effective detector sensitivity.

The quadratic reconstruction technique described reduces the degradation of energy resolution due to charge spreading in bipixel events allowing greater sensitivity compared to using only isolated events and improved energy resolution compared to the CSA technique.

The energy resolution achievable with quadratic reconstruction can be improved if events that are due to X-ray fluorescence are excluded from analysis. However, exclusion of these events represents an additional trade-off between energy resolution and sensitivity. The effects of fluorescence events will vary as false positives become more or less likely, and the use of variable windows for different target isotopes may further increase performance.

Further work is needed to test the quadratic reconstruction technique with a range of detector designs including different detector materials, thicknesses, and pixel sizes. This may lead to improved performance for a range of detectors, and could improve understanding of charge sharing in small pixel semiconductors. In addition, the development of charge transport simulations for these detectors including both hole and electron transport, along with further experimental work in setups where both holes and electrons are measured, will allow deeper connections to be drawn between charge transport effects and the generation of multipixel events.

The use of this technique for thicker detectors, with a higher counting efficiency but more significant depth of interaction effects, could improve utility for medical imaging. The smaller pixel size also opens up the possibility of improved spatial resolution compared to existing clinical CdZnTe systems — although both spatial resolution and system sensitivity will heavily depend on collimator design.

Acknowledgements

This work was supported by a Science and Technologies Facilities Council (STFC) grant – CLASP ST/M007820/1 – and fellowship – ST/R00501X/1. K.A. Koch-Mehrin is supported by a University of Leicester LISEO studentship. The event analysis code is based on work originally carried out by GM Hansford, University of Leicester. The authors would like to acknowledge the contributions of LK Jambi, King Saud University, and WR McKnight and J Michalowska, University of Leicester, to data collection and analysis. This research used the ALICE High Performance Computing Facility at the University of Leicester.

Declaration of competing interest

The authors declare that there are no known conflicts of interest associated with this publication.

References

- [1] A. Owens, *Compound Semiconductor Radiation Detectors*, CRC Press, Taylor & Francis Group, 2012.
- [2] E. Goshen, L. Beilin, E. Stern, T. Kenig, R. Goldkorn, S. Ben-Haim, Feasibility study of a novel general purpose CZT-based digital SPECT camera: Initial clinical results, *EJNMMI Phys.* 5 (1) (2018) 6.
- [3] N. Gehrels, The swift gamma-ray burst MIDEX, *AIP Conf. Proc.* 526 (2000) 671–680.
- [4] E. Kamieniecki, Effect of charge trapping on effective carrier lifetime in compound semiconductors: High resistivity CdZnTe, *J. Appl. Phys.* 116 (19) (2014) 193702.
- [5] H. Toyama, A. Higa, M. Yamazato, T. Maehama, R. Ohno, M. Toguchi, Quantitative analysis of polarization phenomena in CdTe radiation detectors, *Japan. J. Appl. Phys.* 45 (11R) (2006) 8842.
- [6] H. Barrett, J. Eskin, H. Barber, Charge transport in arrays of semiconductor gamma-ray detectors, *Phys. Rev. Lett.* 75 (1) (1995) 156.
- [7] Z. He, Review of the Shockley–Ramo theorem and its application in semiconductor gamma-ray detectors, *Nucl. Instrum. Methods Phys. Res. A* 463 (1–2) (2001) 250–267.
- [8] M.E. Myronakis, D.G. Darambara, Monte Carlo investigation of charge-transport effects on energy resolution and detection efficiency of pixelated CZT detectors for SPECT/PET applications, *Med. Phys.* 38 (1) (2011) 455–467.

- [9] M. Veale, L. Jones, B. Thomas, P. Seller, M. Wilson, K. Iniewski, Improved spectroscopic performance in compound semiconductor detectors for high rate X-ray and gamma-ray imaging applications: A novel depth of interaction correction technique, *Nucl. Instrum. Methods Phys. Res. A* (2019).
- [10] M. Veale, S. Bell, D. Duarte, A. Schneider, P. Seller, M. Wilson, K. Iniewski, Measurements of charge sharing in small pixel CdTe detectors, *Nucl. Instrum. Methods Phys. Res. A* 767 (2014) 218–226.
- [11] L. Abbene, G. Gerardi, F. Principato, Digital performance improvements of a CdTe pixel detector for high flux energy-resolved X-ray imaging, *Nucl. Instrum. Methods Phys. Res. A* 777 (2015) 54–62.
- [12] S.R. Cherry, J.A. Sorenson, M.E. Phelps, *Physics in Nuclear Medicine*, third ed., Elsevier, PA, USA, 2003.
- [13] E. Hindié, Ö. Ugur, D. Fuster, M. O'Doherty, G. Grassetto, P. Ureña, A. Kettle, S.A. Gulec, F. Pons, D. Rubello, 2009 EANM parathyroid guidelines, *Eur. J. Nucl. Med. Mol. Imaging* 36 (7) (2009) 1201–1216, <http://dx.doi.org/10.1007/s00259-009-1131-z>.
- [14] E. Hindié, D. Melliere, C. Jeanguillaume, L. Perlemuter, Parathyroid imaging using simultaneous double-window recording of technetium-99m-sestamibi and iodine-123, *J. Nucl. Med.* 39 (6) (1998) 1100.
- [15] R. Laforest, D. Beyder, W. Scheve, D. Silvestros, N. Shmuel, G. Kovalski, Dual nuclide quantitative imaging with $^{99m}\text{Tc}/^{123}\text{I}$ using CZT gamma camera, *J. Nucl. Med.* 58 (Suppl. 1) (2017) 742.
- [16] P. Fan, B.F. Hutton, M. Holstenson, M. Ljungberg, P. Hendrik Pretorius, R. Prasad, T. Ma, Y. Liu, S. Wang, S.L. Thorn, Scatter and crosstalk corrections for $^{99m}\text{Tc}/^{123}\text{I}$ dual-radionuclide imaging using a CZT SPECT system with pinhole collimators, *Med. Phys.* 42 (12) (2015) 6895–6911.
- [17] L. Abbene, G. Gerardi, F. Principato, M. Bettelli, P. Seller, M.C. Veale, O. Fox, K. Sawhney, N. Zambelli, G. Benassi, Dual-polarity pulse processing and analysis for charge-loss correction in cadmium–zinc–telluride pixel detectors, *J. Synchrotron Radiat* 25 (4) (2018).
- [18] L. Jones, P. Seller, M. Wilson, A. Hardie, HEXITEC ASICa pixellated readout chip for CZT detectors, *Nucl. Instrum. Methods Phys. Res. A* 604 (1–2) (2009) 34–37.
- [19] M. Veale, P. Seller, M. Wilson, E. Liotti, HEXITEC: A high-energy X-ray spectroscopic imaging detector for synchrotron applications, *Synchrotron Radiat. News* 31 (6) (2018) 28–32.
- [20] IDL (Interactive Data Language) 8.2.2, Exelis Visual Information Solutions, Boulder, CO, 2013, <http://www.exelisvis.com/docs/home.html>.
- [21] E. Kalemci, Matteson J.L., Investigation of charge sharing among electrode strips for a CdZnTe detector, *Nucl. Instrum. Methods Phys. Res. A* 478 (3) (2002) 527–537, [http://dx.doi.org/10.1016/S0168-9002\(01\)00892-0](http://dx.doi.org/10.1016/S0168-9002(01)00892-0), <http://www.sciencedirect.com/science/article/pii/S0168900201008920>.
- [22] M.J. Berger, J. Hubbell, S. Seltzer, J. Chang, J. Coursey, R. Sukumar, D. Zucker, K. Olsen, XCOM: Photon cross sections database, *NIST Stand. Ref. Database* 8 (1998) 87–3597.
- [23] J. Scuffham, M. Wilson, P. Seller, M. Veale, P. Sellin, S. Jacques, R. Cernik, A CdTe detector for hyperspectral SPECT imaging, *J. Instrum.* 7 (08) (2012) P08027.
- [24] B.F. Hutton, K. Erlandsson, K. Thielemans, Advances in clinical molecular imaging instrumentation, *Clin. Transl. Imaging* 6 (1) (2018) 31–45, <http://dx.doi.org/10.1007/s40336-018-0264-0>.